Job-Sharing Charge Storage in a Mixed Ion/Electron Conductor Electrode towards Ultrafast Na Storage

Jing Zhang[1], Jiliang Zhang[1], Vincent Wing-hei Lau[1], Haihua Wang[2*], Gi-Hyeok Lee[3], Kai Zhang[4], Mihui Park[3], Liang Fang[3], and Yong-Mook Kang[1*]

[1]Department of Materials Science and Engineering, Korea University, Seoul 02841, Republic of Korea

[2]College of Chemistry and Chemical Engineering, Shaanxi University of Science and Technology, Xi'an, 710021, PR China

[3]Department of Energy and Materials Engineering, Dongguk University-Seoul, Seoul 04620, Republic of Korea

[4]Key Laboratory of Advanced Energy Materials Chemistry (Ministry of Education), Renewable Energy Conversion and Storage Center, College of Chemistry, Nankai University, Tianjin 300071, China

E-mail: dake1234@korea.ac.kr (Y.-M. Kang), whh@sust.edu.cn (H. Wang)

Table of Contents

Supplementary Tables

Supplementary References

Methods

Synthesis of amorphous FeOOH NDs/rGO

The amorphous FeOOH NDs/rGO was prepared by a liquid phase reaction method modified from a previous report.[1] Typically, 40 mg of GO powder was dispersed into 40 mL of absolute ethanol by sonication for 30 min. 270 mg of $FeCl_3 \cdot 6H_2O$ in 30 mL of absolute ethanol was then mixed with the GO dispersion. After stirring for 1 h, 245 mg of NH_4HCO_3 was added into the mixed solution. The reaction was maintained for 20 h at room temperature with continuous stirring. The product was washed by deionized water for 3 times after centrifugation and then vacuum dried at 60 °C for 12 h.

Synthesis of FeHCF NDs/rGO

In a typical process, 30 mg of as-prepared FeOOH NDs/rGO powder was dispersed into 50 mL distilled water. After sonication for 30 min, 2 mg of ascorbic acid and 2 g of NaCl were added. The solution was stirred for 1 h, and then 484 mg of $Na_4Fe(CN)_6 \cdot 10H_2O$ was added. After stirring for 12 h, the precipitate was collected by centrifugation and washed with distilled water and ethanol for 3 times. The product was successively dried under vacuum at 60 °C for 8 h and at 120 °C for 24 h. For comparison, FeHCF MCs/rGO was synthesized following the same experimental condition, except that 50 mg of ascorbic acid was added. For the synthesis of FeHCF NDs/rGO with different mass fractions of FeHCF NDs, different amounts of $FeCl_3 \cdot 6H_2O$ (27, 135, 540, 810, 1080, and 1350 mg) were used to synthesize FeOOH NDs/rGO precursors. The subsequent synthesis steps are the same as the above typical process.

Synthesis of NTP@C

NTP was synthesized by a modified hydrothermal process, as previously reported.[2] Typically, 1.5 g of NaH_2PO_4, 1.5 g of anatase TiO_2 powder, and 1.5 mL of H_3PO_4 (98wt%) were ground in a mortar for 2 min. Then 2 mL of deionized (DI) water was added and ground for 5 min. The mixture was transferred

into a 50 mL Teflon-lined autoclave, sealed, and heated at 150 °C for 6 h. The products were washed with DI water and ethanol several times and then dried at 60 °C overnight. For the synthesis of NTP@C, 2 g of glucose was dissolved into 20 g of acetone, followed by the addition of 1g of NTP. The solution was stirred and heated at 80 °C to evaporate the acetone completely. The obtained powder was ground and calcined at 600 °C for 4h under an Ar atmosphere.

Material characterizations

The morphologies of the materials were characterized through SEM (JSM-6700F field-emission, JEOL) with an energy-dispersive spectrometer (Oxford Instruments, X-Max^N) for EDS and TEM (JEM-2100F, JEOL). N_2 adsorption-desorption isotherms were measured at 77 K using a MicrotracBEL BELSORP-Mini II instrument. Elemental weight proportion was quantified by inductively coupled plasma atomic emission spectroscopy (ICP-AES) (OPTIMA 8300, PerkinElmer). Thermogravimetric analysis (TGA) was conducted on an SDT Q600 thermal gravimetric analyzer (TA Instruments). XRD patterns were collected on a Rigaku Ultima IV X-ray diffractometer operating at 40 kV and 30 mA with Cu *Kα* radiation. XPS was performed on a PHI 5000VersaProbe ULVAC-PHI system with a monochromatic Al *Kα* X-ray source. Raman spectra were collected with a Horiba LabRam ARAMIS IR^2 system. XAS was carried out at the 10C beamline at Pohang Accelerating Laboratory (PAL) in the Republic of Korea.

Electrochemical characterizations

The working electrodes were made by mixing the active materials, super P, and polyvinylidene fluoride (PVDF) at a mass ratio of 8:1:1 in N-methyl-2-pyrrolidone (NMP). The slurry was coated onto an Al foil and heated at 120 °C for 5 h under vacuum. Electrodes were assembled in 2032 coin-type testing cells; cell assembly was performed in an Ar-filled glove box using 1 M $NaPF_6$ in ethylene carbonate/diethyl

carbonate (EC/DEC, 1:1 by volume) as the electrolyte and glass fiber (Whatman) as the separator. For the half cell, a piece of Na foil was used as the counter electrode. The FeHCF NDs/rGO//NTP@C full cell was fabricated by FeHCF NDs/rGO as cathode material and NTP@C as anode material. The NTP@C electrode was prepared by the same method as the cathode except that Cu foil was used as the current collector. Cyclic voltammetry (CV) was performed on a WBCS battery cycler (WonATech). Galvanostatic charge-discharge measurement and galvanostatic intermittent titration technique (GITT) analysis were conducted on a NEWARE battery tester. Electrochemical impendence spectra (EIS) were collected on an electrochemical interface & impedance analyzer (IVIUMSTAT) with an AC perturbation of 5 mV in the frequency range of 100 kHz-100 mHz.

Defect thermodynamics of job-sharing storage

The expression of a_{Na} as a function of Q in the contact of a Frenkel-disordered ionic conductor and a pure semiconductor based on the defect chemistry is given by[3]

$$a_{Na} = \frac{(Q+\sqrt{Q^2+8\varepsilon_\alpha\varepsilon_0 RT\sqrt{K_F}})^2(Q+\sqrt{Q^2+8\varepsilon_\beta\varepsilon_0 RT\sqrt{K_B}})^2}{64K_{Na}\varepsilon_\alpha\varepsilon_\beta(\varepsilon_0 RT)^2} e^{\frac{FsQ}{\varepsilon_{\alpha\beta}\varepsilon_0 RT}} \quad (1)$$

Here ε_α and ε_β are the dielectric constants of phases α and β, and $\varepsilon_{\alpha\beta}$ denotes the mean dielectric constant, K_F and K_B are the ionic and electronic mass action constants in phases α and β, respectively, K_{Na} is mass action law constant for the electrochemical reaction, *s* is the width of the charge-free zone, and R, T, F, ε_0 have their usual meanings.

The job-sharing mechanism shows three storage modes:

(1) Intrinsically controlled storage. a_{Na} is determined by the intrinsic characteristics of the contact phases. This mode usually appears in low Q step ($Q^2 \ll 8\varepsilon_\alpha\varepsilon_0 RT\sqrt{K_F}$ and $Q^2 \ll 8\varepsilon_\beta\varepsilon_0 RT\sqrt{K_B}$) and a_{Na} maintains as a constant.

(2) Diffusive-layer controlled storage. With increasing charge stored but is still low enough for the exponential term to be essentially unity, the behavior then emphasizes the diffuse double layer part. The power law factor Q^4 will dominate; the factor will be Q^3 for the strong electronic conductor. In this storage mode, the stored charge is mostly contributed by the majority carrier in the diffuse layer.

(3) Rigid-layer controlled storage. With increasing Q, the space charge layer accumulates numerous charges. The system behaves like an electrostatic capacitor (equilibrium potential is proportional to the capacity), and the stored capacity is mostly contributed by the charges at the boundary. The exponential function exp (kQ) dominates the storage. Note that the charge storage of the job-sharing mechanism is at the solid/solid interface, while for conventional supercapacitors, the matter is stored at a solid/liquid interface. Additionally, ln Q vs. ln a_{Na} is bent for storage dominated by the rigid-layer mode due to the exponential function, but shows a linear relationship for bulk storage.

Calculation of the size-dependence of insertion capacity

Naturally, size confinement can bring adverse effects. One big issue is the decrease of insertion capacity for ion insertion type framework, especially for small-nanosized systems. To calculate the insertion capacity, we simplify the Prussian blue particle as an ideal cube composed of Fe–C≡N–Fe cubic framework unit, as shown in Supplementary Fig. 13a. One unit can store one Na^+ ion. Assuming the cube is composed of n^3 single framework units, the cube side length l equals n multiplied by the length of a single framework unit. In this assumption, the number of Na^+ ions that can be inserted is n^3. Surface atoms should be considered since the atom occupancy on the surface is different from that in the bulk: surface vertex Fe contributes one atom to a unit, surface edge Fe contributes 1/2 atom to a unit, surface face Fe contributes 1/4 atom to a unit, internal Fe contributes 1/8 atom to a unit. Similarly, surface edge C (or N) contributes one atom to a unit, surface face C (or N) contributes 1/2 atom to a unit, internal C (or N) contributes 1/4 atom to a unit. Hence, with more surface atoms exposed, the more atoms contribution to

the unit. Overall, the atomic ratios of Na to other elements are changed. For the cube with n^3 units, the number of Na atoms is n^3, the number of Fe atoms is $(n+1)^3$, the number of C (or N) atoms is $3n(n+1)^2$. The molecular formula can be written as $Na_{n^3}Fe_{(n+1)^3}(CN)_{3n(n+1)^2}$. Therefore, the molar mass of the cube is M = $23n^3 + 56(n+1)^3 + 78n(n+1)^2$. The insertion capacity C_0 (mAh g^{-1}) is calculated based on the following formula:

$$C_0\left(\frac{mAh}{g}\right) = F\left(\frac{C}{mol}\right) \times n_{Na} \times \frac{1}{M}\left(\frac{mol}{g}\right) \times \frac{1}{3.6}\left(\frac{mAh}{C}\right) \quad (2)$$

where F is Faraday constant, n_{Na} is the number of Na ions, which in our case is n^3. Hence, the insertion capacity is calculated to be:

$$C_0 = \frac{53611n^3}{46n^3+112(n+1)^3+156n(n+1)^2} \quad (3)$$

The side length of every unit is ≈0.5 nm, and the side length of the cube (l) satisfies the equation $l = 0.5n$. Therefore, C_0 can be calculated as a function of l by

$$C_0 = \frac{53611l^3}{46l^3+14(2l+1)^3+39l(2l+1)^2} \quad (4)$$

Based on this, we calculated the size-dependence of insertion capacity in an ideal situation (Fig. 3i). The insertion capacity can reach 170 mAh g^{-1} (theoretical capacity for bulk) when the length of the cube is above 100 nm, but decreases dramatically with size reduction. Hence, for cubes of dimension 10nm×10nm×10nm, which is the size of the PBA in FeHCF NDs/rGO based on the TEM analyses, the insertion capacity is 154 mAh g^{-1}, a loss of nearly 20 mAh g^{-1} compared to bulk crystals. Similar explanation can partially rationalize why some materials (e.g., $LiCoO_2$) present an attenuated capacity after downsizing.[4,5] However, FeHCF NDs/rGO maintains a high initial discharge capacity of 132 mAh g^{-1} similar to the bulk material (131 mAh g^{-1} for FeHCF MCs/rGO) at a low current density of 0.2 C, which is credited to the high interface storage as mentioned above.

Calculation of *b*-value

Supplementary Fig. 15a, b shows the CVs of the two electrodes at various scan rates (from 0.1 mV s^{-1} to 2 mV s^{-1}). The relationship between the peak current (i) and scan rate (v) that reflects the surface/interface capacitive characteristic proportion can be expressed by:

$$i = av^b \quad (5)$$

The b-value is calculated through linear fitting of the log (v)–log (i) plots for both cathodic and anodic peaks (Fig. 4e). With this analysis, for b = 0.5 is indicative of pure diffusion control, while b = 1 is indicative of pure capacitive process. The high b-values of 0.86 and 0.89 for FeHCF NDs/rGO indicate both diffusion-controlled and capacitive processes in the Na storage mechanism, of which the latter is predominant.[6] In contrast, FeHCF MCs/rGO shows two different b-values of 0.54 and 0.61 at a low sweeping rate, and 0.75 and 0.85 at a high sweeping rate. Hence, Na storage is largely diffusion-controlled at a low scan rate but is more capacitive with increasing scan rate.

Calculation of surface/interface contribution

The proportion of charge stored at the surface/interface can be calculated by separating the capacitive current (k_1v) and battery current ($k_2v^{1/2}$) in the equation:

$$i = k_1v + k_2v^{1/2} \quad (6)$$

Supplementary Fig. 15c presents an example of surface/interface behavior for FeHCF NDs/rGO at 0.2 mV s^{-1}, which is highlighted in the shaded area. The contribution ratios of the two electrodes at various scan rates are shown in Fig. 4f. The capacitive contribution of FeHCF NDs/rGO at a low sweep rate is as high as 72.2% at 0.1 mV s^{-1} and 80% at 0.2 mV s^{-1}, suggesting that even at low scan rate the surface/interface capacitive characteristic is remarkable. This agrees well with the CV and

charge/discharge curves in Fig. 3 and compensated for the loss of capacity due to downsizing. The capacitive contribution slightly increases with increasing sweep rate. In contrast, FeHCF MCs/rGO exhibits lower capacitive contribution of only 45.3% at 0.1 mV s^{-1} and 47.5% at 0.2 mV s^{-1}, suggesting a diffusion-controlled storage mode at low rate due to its less exposed surface. Although the capacity provided by surface storage is low, its contribution still significantly increases with the increase of sweep rate, revealing that at a high rate diffusivity is the bottleneck to capacity contribution.

GITT measurements

The GITT measurements were carried out by applying a current pulse of 20 mA g^{-1} for 10 min and then left on open circuit for 1 h. Prior to GITT tests, the electrodes were first cycled at 1 C for 10 cycles to reach a stable state. The rate of Na ion diffusion is determined by the change in voltage with time in a GITT test. The D_{Na} value can be calculated by the following equation:[7,8]

$$D = \frac{4}{\pi\tau}\left(\frac{m_B V_M}{M_B S}\right)^2\left(\frac{\Delta E_s}{\Delta E_\tau}\right)^2 \quad (7)$$

where, τ is the duration of the current pulse (s), m_B, M_B, and V_M represent the mass (g), molar mass (mol), and molar volume ($cm^3 \cdot mol^{-1}$) of the active material, S is the electrode-electrolyte interfacial area (cm^2), ΔE_s denotes the steady-state potential change arising from the current pulse (V), and ΔE_τ represents the change in the overall voltage under galvanic conditions, neglecting the IR drop (V).

Supplementary Note 1. Discussion of size-dependent lattice expansion.

The synthesis of FeHCF MCs/rGO used more ascorbic acid than for the ND counterpart. Because ascorbic acid can reduce Fe^{3+} to Fe^{2+}, FeHCF MCs/rGO is expected to show higher content of Na. However, FeHCF NDs/rGO has both higher Na and crystal water content than FeHCF MCs/rGO. This phenomenon leads to a significant correlation of the crystal structure with the size effect, that is lattice

expansion for the FeHCF NDs/rGO sample. The lattice expansion is commonly ascribed to the existence of low valence metal in oxides (such as Co^{2+} in $LiCoO_2$[4] and Ce^{3+} in CeO_2[9]) or surface adsorbents (such as O_2 or CO_2[10]). Although some literature has proposed a quantitative description of surface-induced lattice variation,[11,12,13] it is almost impossible to derive explicit dependencies between the lattice parameter and the particle size so far due to the complexities of various materials.[14] Here, we consider this from a fundamental view: two opposing forces, including long-range Coulombic and short-range atomic interactions, exist in a crystal, which causes attractive and repulsive pair potentials within the crystal.[15] The attractive interaction forms a positive surface stress, resulting in a positive (i.e. compressive) pressure and vice versa. The attractive and repulsive energy balance in the bulk material. For the surface atoms, although both energies are weakened, however, this balance will be broken due to the chemical environment being different from the bulk.[15] Therefore, for the reduced crystallite size with a high surface-to-volume ratio, the lattice variation is determined by the competition between the relative attractive and repulsive excess energies. The lattice variation can be defined by the following theoretical model proposed by Diehm et al.[16]

$$\frac{n_{tot}}{n_{sur}} \frac{d\frac{E_{tot}}{n_{tot}}}{da} = -\omega \frac{d}{da} \varepsilon_b^A \tag{8}$$

where a is the interatomic distance, n_{tot} and n_{sur} are the number of total and surface atoms, respectively, E_{tot} is the total energy of the particle, ε_b^A is the attractive energy per atom in the ideal bulk, ω substitutes α–β in which α and β replace the negative proportion of excess surface energy to excess bulk energy per atom for the attractive and repulsive energy, respectively. The sign of the total energy derivative is determined solely by the value of ω because $d(\varepsilon_b^A)/da$ is positive, which results in lattice expansion when $\alpha > \beta$ (e.g., $LiCoO_2$,[4] $BaTiO_3$,[17] and $MnCr_2O_4$,[18]) and contraction when $\alpha < \beta$ (e.g., $LiMn_2O_4$,[19] NiO,[20] and Pt[21]). Although the quantitative prediction is hard to carry out by this simple model, it allows us to

understand the essence of the lattice change better. In our case, for example, the lattice expansion is caused by the higher excess attractive energy than the excess repulsive energy.

Supplementary Note 2. Discussion of Fe K-edge XANES spectra and Fourier transformed EXAFS spectra.

Fe K-edge XANES spectra (Fig. 2b) of the two samples show different features that are derived from difference of coordination chemistry near Fe atoms. For the nanosized particles, the character of surface atoms significantly affects to the spectra as their ratio is not negligible. Therefore, the different type of ligand bonded with the Fe atoms at the surface and the low crystallinity of NDs caused by nanosizing are attributed to the difference of K-edge region. The intensity of the pre-edge peak is correlated to the degree of distortion of the sublattice.[22] The lower intensity of FeHCF NDs/rGO suggests reduced symmetry of FeC_6 (or FeN_6) octahedra (inset of Fig. 2b), which is caused by the increase of surface unsaturated bonds and defects. The related EXAFS spectra (Fig. 2c) show three apparent peaks in the range of 0.5–2 Å, 2–3 Å, and 4.3–5 Å, attributed to Fe–C(N), Fe–N(C), and Fe–Fe shells, respectively. The peaks of Fe–C and Fe–N shells for FeHCF MCs/rGO have high symmetry with standard cubic characteristic.[23] However, the poorly symmetric peaks of FeHCF NDs/rGO are observed, and the Fourier-transform (FT) magnitude of Fe–Fe shell is reduced, indicating the distortion of the structure. Additionally, the expanded interatomic distance is consistent with the result of XRD.

Supplementary Note 3. Discussion of Raman spectra and XPS spectra.

Raman spectra of the two samples reveal the variation of local structures as well, which have been normalized to account for the different loading amount (Fig. 2d). The spectrum of FeHCF NDs/rGO shows a significant reduction of intensity for the C≡N vibration (including A_{1g} ν_{CN} symmetrical stretching vibration[24] and E_g species of the ν_{CN} vibration[25]) compared with that of FeHCF MCs/rGO. It suggests that

the shrinking of the long-range structure suppresses the vibrational stretching mode of the ultrafine particles.[26] The Fe–CN–Fe/Fe–C ratio is considerably decreased in NDs compared to MCs, which implies the significant change of surface to bulk ratio. Besides, size-induced frequency shift to lower wavenumber is observed (Supplementary Table 2), which is partially caused by the increase of bond distance resulting from lattice expansion and may partly be due to the phonon confinement effect within small grain size.[4,27]

Two kinds of Fe, low-spin (LS) state Fe^{II}(C) and high-spin (HS) state Fe^{III}(N), are fitted from Fe 2p region of the XPS spectrum of FeHCF MCs/rGO (Fig. 2e). Nevertheless, new low-intensity peaks at 706.19 eV and 718.88 eV, which are referred to as the 'pre-peak', appears at lower binding energy in the Fe $2p_{3/2}$ and Fe $2p_{1/2}$ envelopes. These peaks indicate a lower oxidation state than typical LS Fe^{II}(C), which may be caused by abundant surface-exposed Fe^{II}–C≡N group with Fe^{III} defects in neighboring sites that increases the electron density of Fe^{II}(C) without the share of Fe^{III}(N).[28] Importantly, FeHCF NDs/rGO shows a peak shift to lower binding energy compared with FeHCF MCs/rGO, revealing Fe in Prussian blue attracts electrons from the π–π conjugated system of graphene.[29] It further indicates the interaction within the close contact interface of the composite. N 1s spectra (Fig. 2f) can be fitted to three peaks: Fe^{II}–C≡N–Fe^{III} bonds at 397.7 eV for the bulk structure, the chemically new configuration at 399.8 eV due to the interaction with graphene layers, and Fe^{II}–C≡N bonds at 402.4 eV for the surface structure.[30] The relative intensities of N(399.8 eV) and N(402.4 eV) to N(397.7 eV) for FeHCF NDs/rGO are both increased as compared with FeHCF MCs/rGO, revealing more significant impact from graphene and higher proportion of the uncoordinated Fe^{II}–C≡N group. The results are consistent with the Fe 2p spectrum.

Supplementary Note 4. Discussion of CV and charge/discharge profiles.

Fig. 3a, b show CV of FeHCF MCs/rGO and FeHCF NDs/rGO at 0.1 mV s^{-1} in the voltage range of 2–4.2 V. The CV of FeHCF MCs/rGO has the typical profile of bulk sodium iron hexacyanoferrates with two redox couples: 2.91/3.38 V for high-spin Fe^{HS}(N) and 3.65/3.93 V for low-spin Fe^{LS}(C). After downsizing the particles, the CV of FeHCF NDs/rGO displays a different electrochemical characteristic. The redox peaks have lower current. Only one pair of obvious redox peaks at 2.92/3.4 V can be observed. Importantly, the capacity at lower potential increases, leading to an enlarged coverage area of CV profile. This phenomenon is attributed to the surface or interface capacitive behavior of the ultrafine particle, which overlaps the redox peaks.[4] The galvanostatic charge/discharge profile of FeHCF MCs/rGO at 0.2 C (1 C = 170 mA g^{-1}) in Fig. 3c presents two platforms of Fe^{HS}(N) and Fe^{LS}(C), which are consistent with the CV. In contrast, the charge/discharge profile of FeHCF NDs/rGO shows a different shape with a narrower miscibility gap. From a thermodynamic point of view, the surface atoms in size-confined particles have excessive surface free energy that leads to an extra effect on Na chemical potential μ_{Na}(small) and thus the cell voltage by[31]

$$\mu_{Na}(small) = \mu_{Na}(bulk) + 2V_{Na}(\gamma/r) \quad (9)$$

Where γ is the surface tension, r is the particle radius, and V_{Na} is the partial molar volume. For the bulk materials, the plateau profiles are flat, whereas they become tilted considering the contribution of the γ/r term for size confinement systems.

Supplementary Note 5. Discussion of ex-situ XRD

As revealed in Fig. 5d, h, at the fully discharged state (2 V), both electrodes present the rhombohedral (R) phase with low crystal symmetry due to the high Na content ($Na_2Fe^{II}Fe^{II}(CN)_6$). Upon Na extraction, the lattice shrinks with the peaks shifting to a high angle, and the cubic (C) phase ($Fe^{III}Fe^{III}(CN)_6$) is obtained at the fully charged state (4.2 V). The phase can turn back to R phase after discharging, indicating a reversible process, which is consistent with previous reports.[32] However, the lattice variation is different.

311 The (202) peak of the R phase for FeHCF MCs/rGO changes from 16.88° to 17.19° after charging, while
312 FeHCF NDs/rGO shows a smaller shift from 16.88° to 17.08° (Fig. 5e, i). The same results are observed
313 for the (404) peak of the R phase shown in Supplementary Fig. 22. These results indicate that FeHCF
314 NDs/rGO shows a smaller lattice variation than FeHCF MCs/rGO. Fig. 5f, j show the normalized volume
315 change within a primitive unit cell for the two electrodes, both of which displayed unit cell volume
316 decrease during Na^+ ion insertion, and *vice versa*. For FeHCF NDs/rGO, the volume decrease is smaller
317 with a variation of below 2.4%, indicative of a highly reversible phase transition. In contrast, FeHCF
318 MCs/rGO exhibited a larger volume change of 4.4%, which is harmful to structural integrity during Na^+
319 insertion/extraction.
320

Supplementary Figures

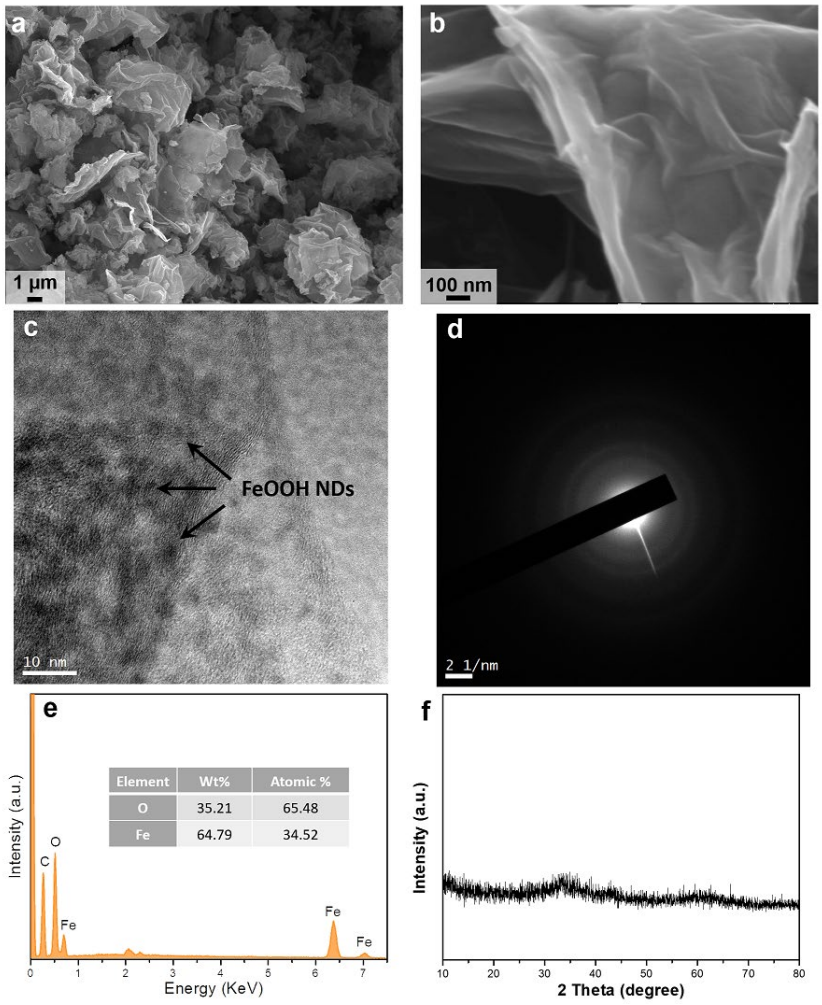

Supplementary Fig. 1 | Characterizations of amorphous FeOOH NDs/rGO. a, **b**, SEM images, **c**, HRTEM image, **d**, SAED pattern, **e**, EDS pattern, and f) XRD pattern.

The formation of FeOOH follows the equation below:[1]

$$FeCl_3 + 3NH_4HCO_3 \rightarrow FeOOH + 3CO_2 + H_2O + 3NH_4Cl \quad (10)$$

Supplementary Figs. 1a, b show the SEM images of FeOOH NDs/rGO. No big and freestanding particles can be observed, indicating the ultra-small nanoparticles fixed on the graphene surface. From the HRTEM image in Supplementary Fig. 1c, the lighter regions can be assigned to the graphene nanosheets, while the darker features are assigned to the FeOOH NDs from the higher atomic mass. Based on this assignment, the FeOOH NDs are uniformly dispersed on the graphene layer with particle size less than 10 nm. The corresponding SAED pattern (Supplementary Fig. 1d) exhibits a broad and diffused halo ring, indicating the amorphous nature of FeOOH NDs with long-range disorder. Supplementary Fig. 1e shows the EDS spectrum for quantifying the atomic ratio of oxygen to iron, which is 65.48:34.52 and is close to the expected 2:1 ratio of FeOOH. The XRD pattern in Supplementary Fig. 1f further illustrates the amorphous nature of the FeOOH, which is consistent with the SAED results.

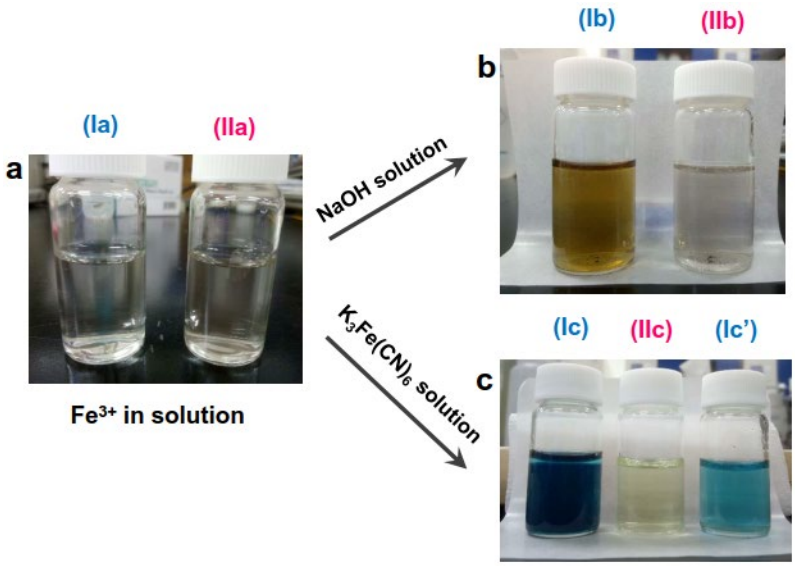

Supplementary Fig. 2 | Digital photos of the solutions under different conditions. a, The supernatants after adding ascorbic acid ((Ia) 50 mg and (IIa) 2 mg) to aqueous dispersion of FeOOH NDs/rGO. **b**, After adding 0.5 mL of 1 M NaOH solution to (Ia) and (IIa), which are respectively notated as (Ib) and (IIb). **c**, After adding 0.5 mL of 1 M $K_3Fe(CN)_6$ solution to (Ia) and (IIa), which are respectively notated as (Ic) and (IIc). The third solution, (Ic'), involved treating solution (Ia) 2 times with 50 mg ascorbic acid before mixing with $K_3Fe(CN)_6$ solution.

To investigate the formation mechanism of FeHCF NDs/rGO and FeHCF MCs/rGO, we designed a comparative experiment. Two dispersions of 30 mg of FeOOH NDs/rGO in 50 mL of DI water were prepared by sonicating for 30 min. To one of these solutions, 50 mg of ascorbic acid was added, and to the other 2 mg. The solutions were stirred for 1 h, and then centrifuged and the supernatant was collected. As shown in (a), the two supernatant solutions were identified as (Ia) and (IIa) for the 50 mg and 2 mg of ascorbic acid added, respectively. Then, 0.5 mL of 1 M NaOH solution was added to 10 mL of these two solutions. The result is shown in (b). The color of (Ib) is much darker than that of (IIb), indicating that solution (Ib) contains a larger amount of dissolved Fe^{3+} due to the larger amount of ascorbic acid (50 mg).

A similar result was obtained by adding 0.5 mL of 1 M $K_3Fe(CN)_6$ solution to the two supernatant solutions (Supplementary Fig. 2c, Ic and IIc), in which the color of (Ic) turned navy blue (formation of $FeFe(CN)_6$) immediately while the color of (IIc) was almost no change. In the third solution (Ic'), the FeOOH NDs/rGO solution with 50 mg of ascorbic acid was kept stirring for 1 h and centrifuged, after which the precipitate was dispersed in another 50 mL of DI water with 50 mg of ascorbic acid for 1 h. This dispersion was then centrifuged and the supernatant was collected and mixed with the $K_3Fe(CN)_6$ solution. The color of the solution turned blue immediately, indicating that FeOOH NDs/rGO could continuously dissociate Fe^{3+} in the situation of 50 mg of ascorbic acid. The above results reveal that a large number of FeOOH dissolve into the solution at a fast rate during the synthesis process of FeHCF NCs/rGO. In contrast, the dissolution rate of FeOOH is extremely slow for the synthesis of FeHCF NDs/rGO.

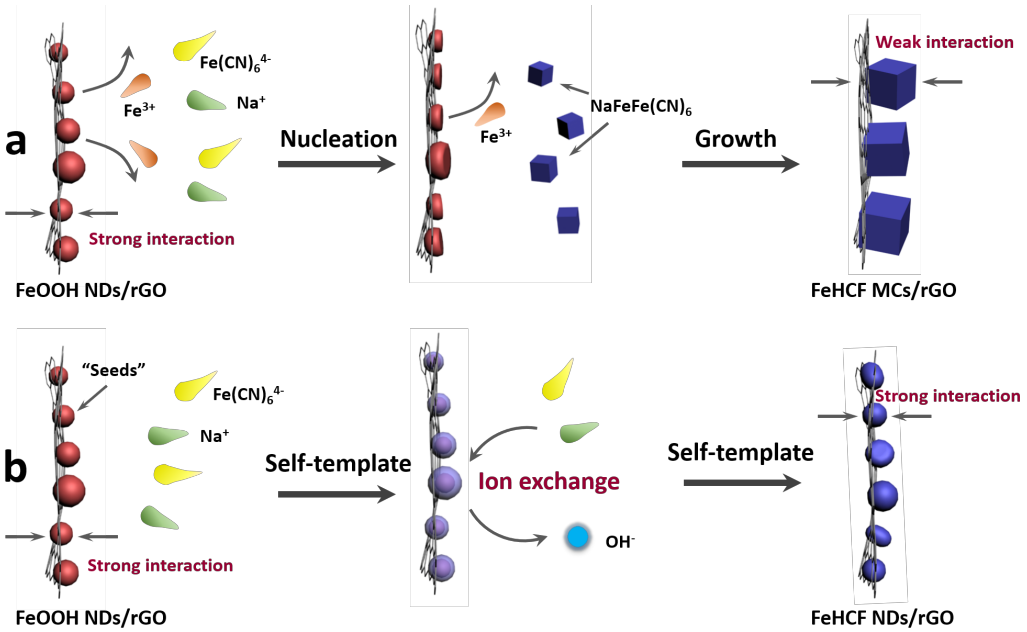

Supplementary Fig. 3 | Possible formation mechanism. a, FeHCF MCs/rGO. **b,** FeHCF NDs/rGO.

In the case of the formation of FeHCF MCs/rGO, as shown in (a), a large amount of Fe^{3+} ions are released from FeOOH NDs/rGO before reaction as disclosed above. After adding $Na_4Fe(CN)_6 \cdot 10H_2O$, $NaFeFe(CN)_6$ nucleates in the solution immediately. As the reaction proceeds, FeOOH continuously dissolves and releases Fe^{3+} ions, and the nuclei of $NaFeFe(CN)_6$ grow to form big nanocubes with regular shape. The FeHCF MCs and graphene sheets show weak interaction because the nucleation of $NaFeFe(CN)_6$ is in the solution, not on the graphene surface. On the other hand, for the synthesis of FeHCF NDs/rGO as illustrated in (b), the FeOOH nanoparticles serve as seeds to achieve a self-templated reaction, that is, an ion exchange reaction with $Fe(CN)_6^{4-}$ and Na^+ ions. The synthesis of FeHCF NDs can be described as in the following equation:

$$FeOOH + Na^+ + Fe(CN)_6^{4-} + H_2O \rightarrow NaFeFe(CN)_6 + 3OH^- \quad (11)$$

The ultra-small FeOOH NDs anchor on the graphene surface throughout the reaction. Therefore, the product FeHCF NDs, as similar to the precursor, show strong interaction with rGO. Meanwhile, this kind of interaction reduces the surface free energy of the ultra-small FeHCF nanoparticles.

383

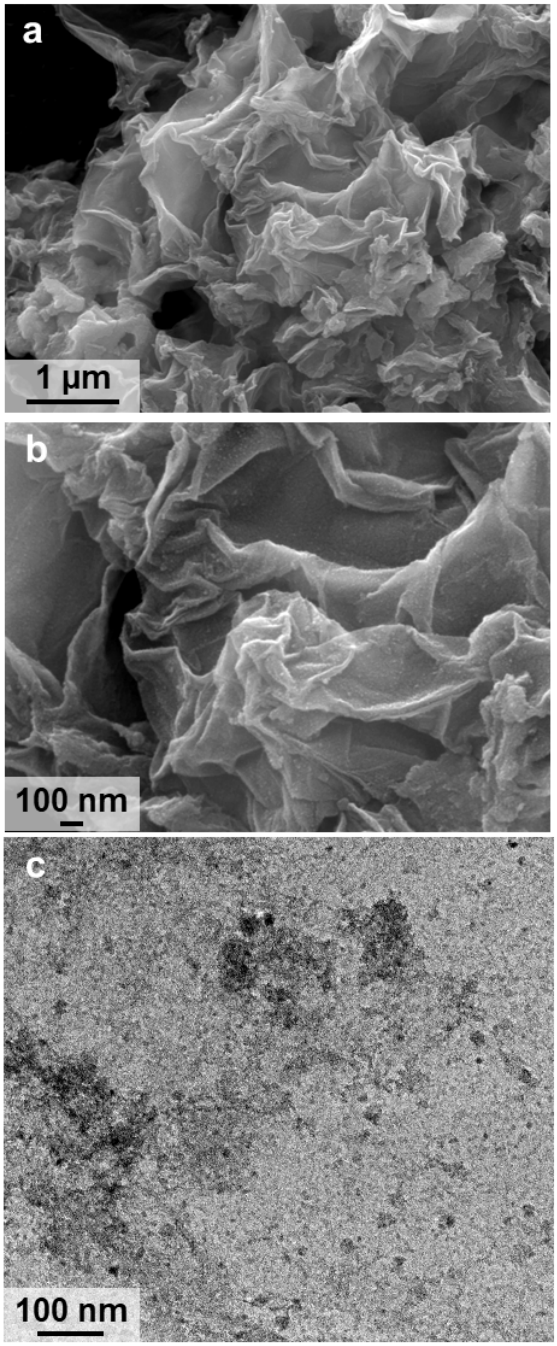

384

385 **Supplementary Fig. 4 | Morphology of FeHCF NDs/rGO. a**, **b**, SEM images. **c**, TEM image.

386

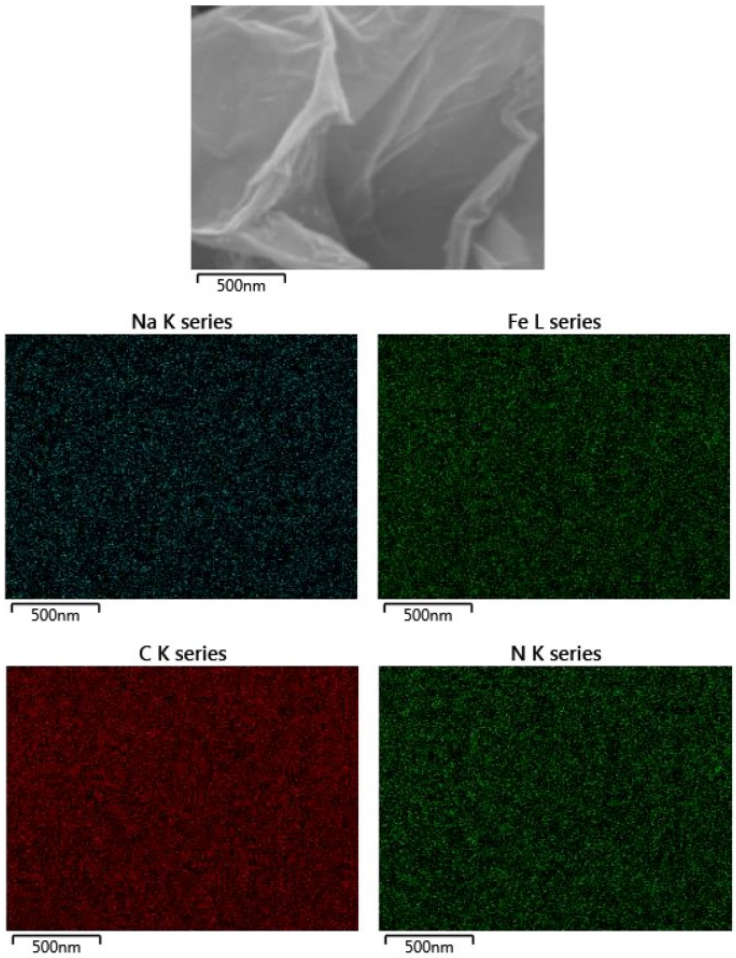

Supplementary Fig. 5 | EDS elemental mapping of Na, Fe, C, and N for FeHCF NDs/rGO.

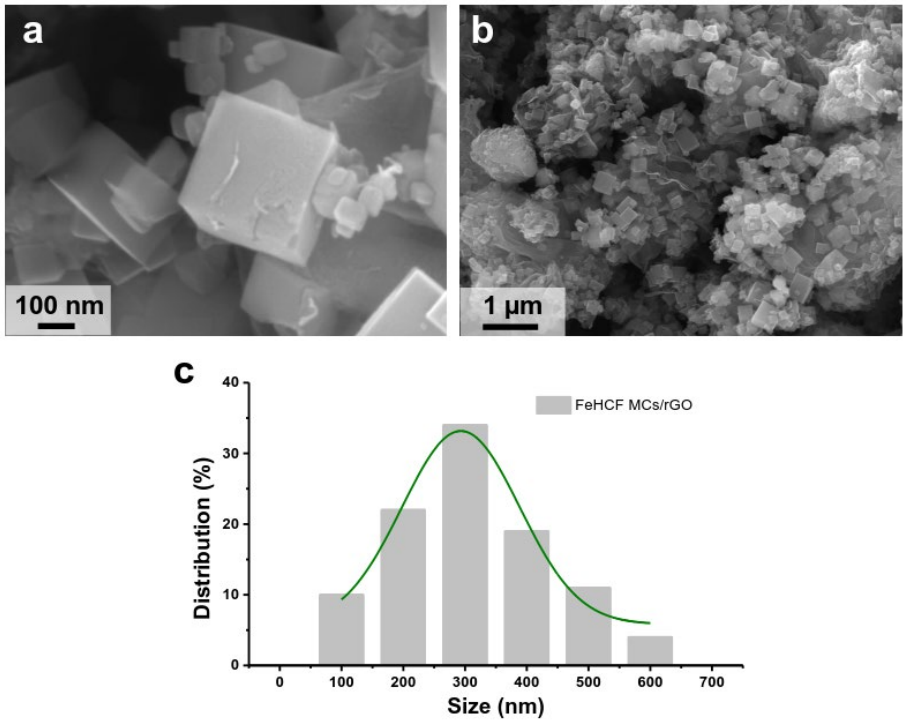

391

392 **Supplementary Fig. 6 | Characterizations of FeHCF MCs/rGO. a**, **b**, SEM images. **c**, particle size

393 distribution of FeHCF MCs (200 particles counted).

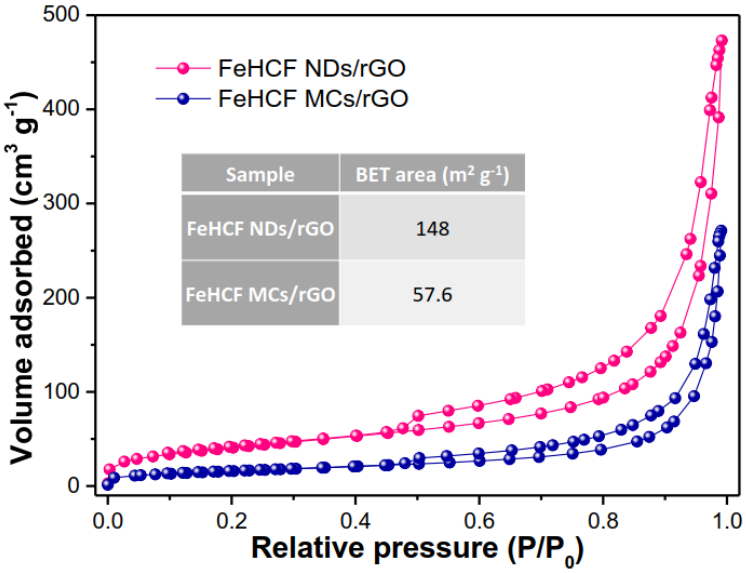

394

395 **Supplementary Fig. 7 | Nitrogen adsorption−desorption isotherm of FeHCF MCs/rGO and FeHCF**

396 **NDs/rGO.** The inset is a table of specific surface area for the two samples.

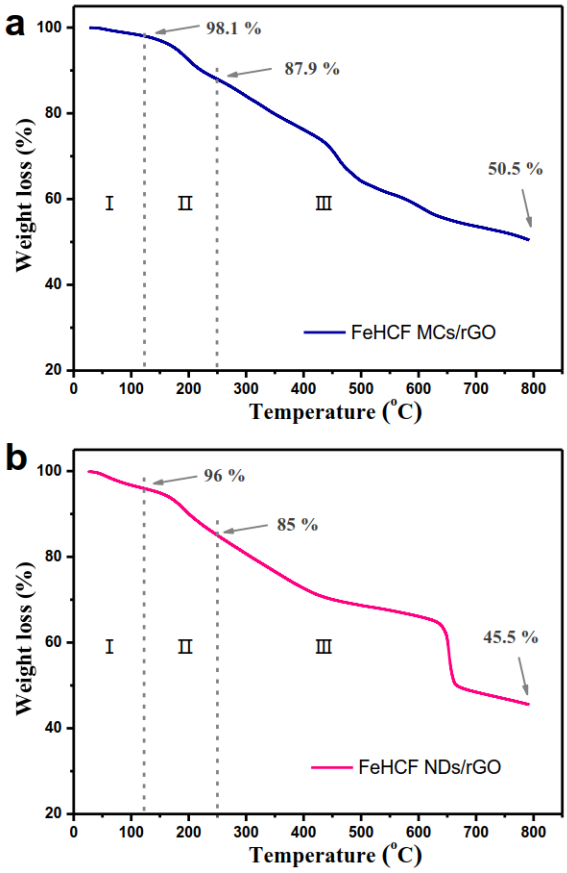

Supplementary Fig. 8 | TGA profiles under N_2 flow. a, FeHCF MCs/rGO. **b**, FeHCF NDs/rGO.

TGA profiles show three decomposition steps: I (25-120 ℃), II (120-250 ℃), III (250-800 ℃). In step I, the mass decrease is assigned to the loss of adsorbed water on the surface of the materials.[33] Based on this assignment, greater water loss in FeHCF NDs/rGO can be attributed to its higher surface area. The mass loss in step II can be attributed to the release of crystal water from the PB structure.[34] 10.2% and 11% of weight loss is observed for FeHCF MCs/rGO and FeHCF NDs/rGO, respectively. The crystal water contents should be 10.4% for FeHCF MCs/rGO and 11.46% for FeHCF NDs/rGO after excluding the adsorbed water weight. Step III represents the decomposition of FeHCF in N_2 atmosphere, which corresponds mainly to a release of cyanide groups from the PB structure accompanied by endothermic

reactions.[35] Rapid mass loss is observed for FeHCF NDs/rGO at high temperature, indicating that FeHCF NDs/rGO shows high thermal stability. Moreover, the similar weight loss in step III (37.4% for FeHCF MCs/rGO and 39.5% for FeHCF NDs/rGO) suggests similar Prussian blue content in the two composites.

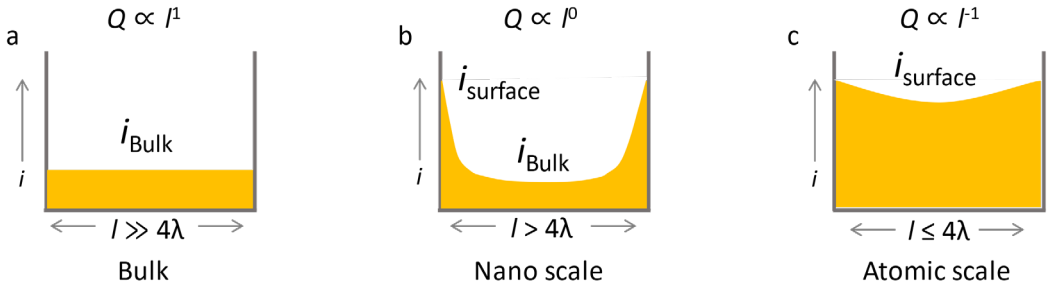

Supplementary Fig. 9 | Space–charge storage capacity as dependent on size. a, bulk. **b**, nano scale. **c**, atomic scale. λ is Debye length.

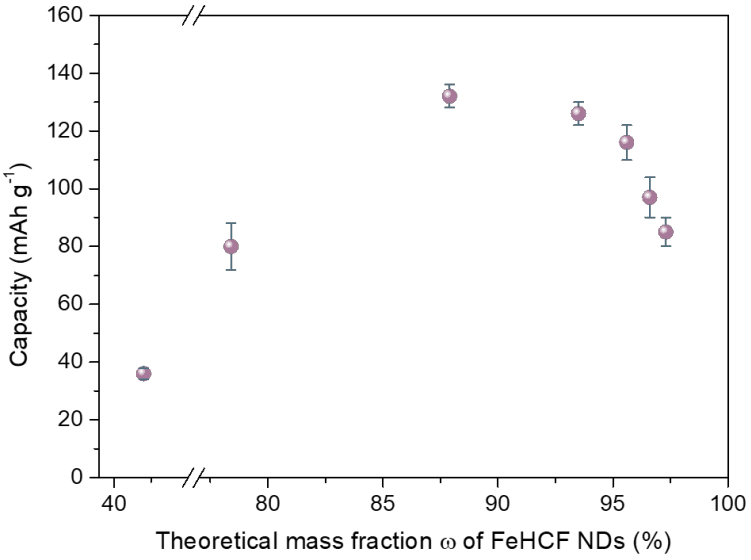

Supplementary Fig. 10 | Storage capacity of the FeHCF NDs/rGO composite as a function of theoretical mass fraction ω of FeHCF NDs in FeHCF NDs/rGO. Error bars show range over three samples.

To verify the interfacial storage, the theoretical mass fraction ω of FeHCF NDs in FeHCF NDs/rGO can be adjusted by changing the amount of reactant $FeCl_3 \cdot 6H_2O$. The capacity of the composite should increase with the increase of ω assuming the interfacial storage is ignored, since the capacity of bare rGO is tiny. However, the storage capacity actually reaches maximum with ω = 87.9% (the value we used for our FeHCF NDs/rGO) then decreases with the increase of ω. This verification suggests that the capacity of the composite is not just provided by the single phase FeHCF NDs or rGO, more importantly, the interfacial storage also makes a great contribution to the total capacity of the composite.

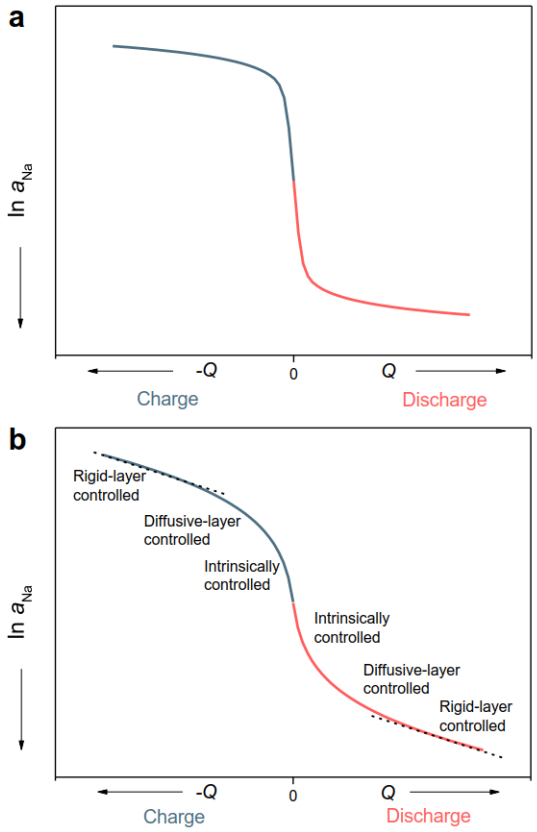

433

434 **Supplementary Fig. 11 | Sodium activity (voltage) versus stored charge *Q* for different storage**

435 **mechanisms. a**, bulk. **b**, job-sharing storage.

436

437

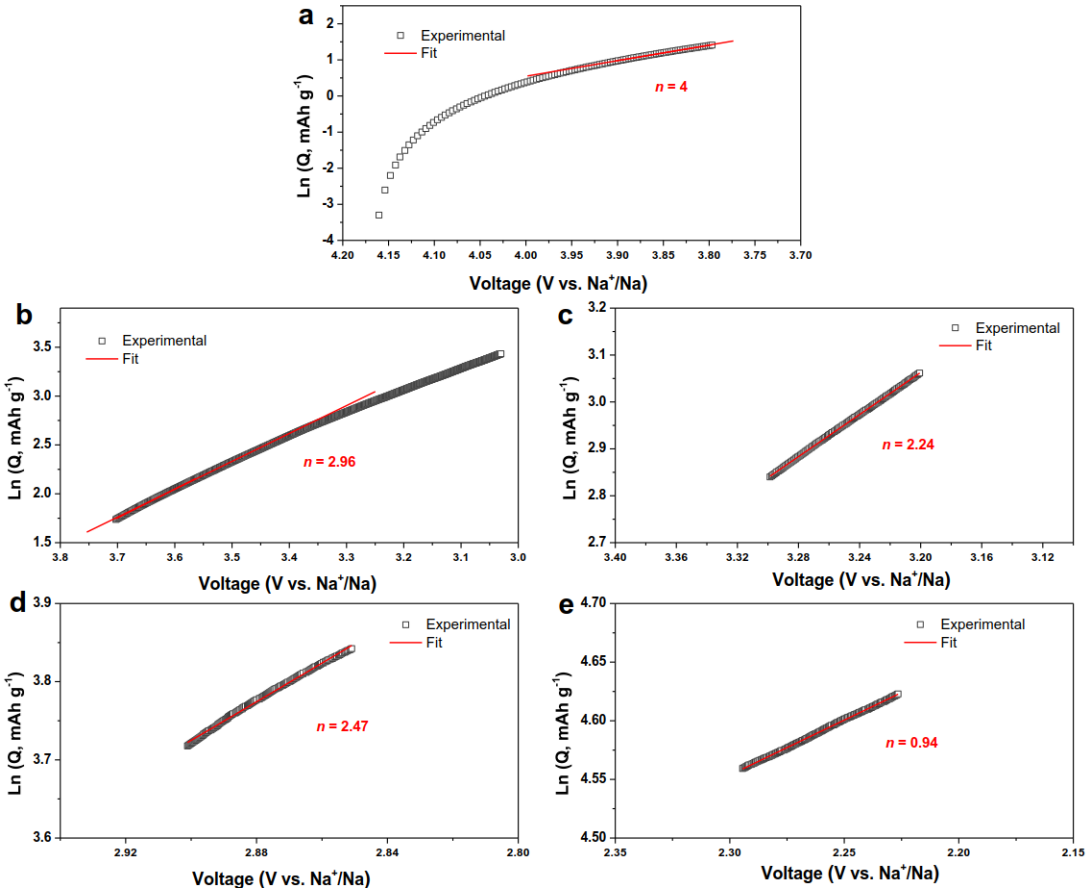

438

439 **Supplementary Fig. 12 | Dependence of sodium interfacial storage on sodium activity at different**

440 **discharge voltages. a,** 3.9−3.8 V**. b,** 3.7−3.5 V**. c,** 3.3−3.2 V**. d,** 2.9−2.85 V**. e,** 2.29−2.22 V**.**

441

442

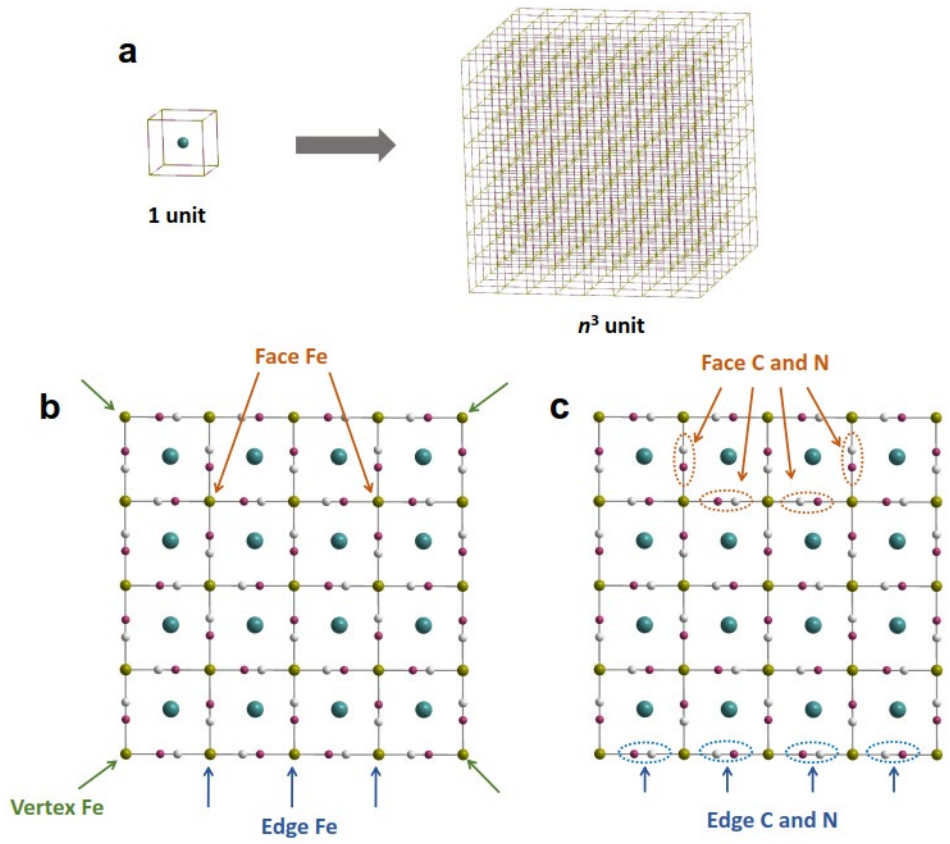

443

444 **Supplementary Fig. 13 | Calculation of insertion capacity in the function of the cube length. a**,

445 Schematic of a cube formed by n^3 units. Atoms at different sites on the exposed surface: (**b**) Fe atoms and

446 (**c**) C and N atoms.

447

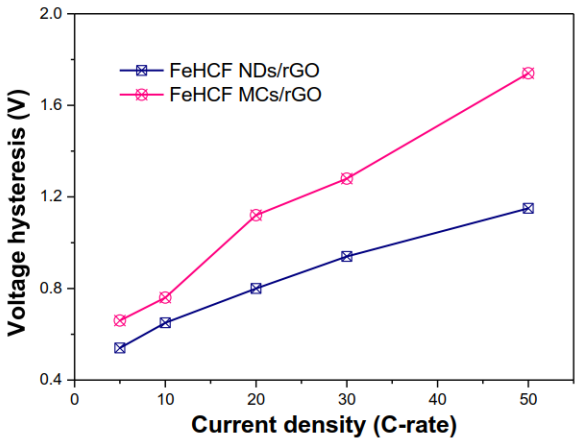

Supplementary Fig. 14 | Voltage hysteresis of electrodes as a function of C-rate. The voltage hysteresis is measured by the difference between the potentials at the half charge and discharge state.

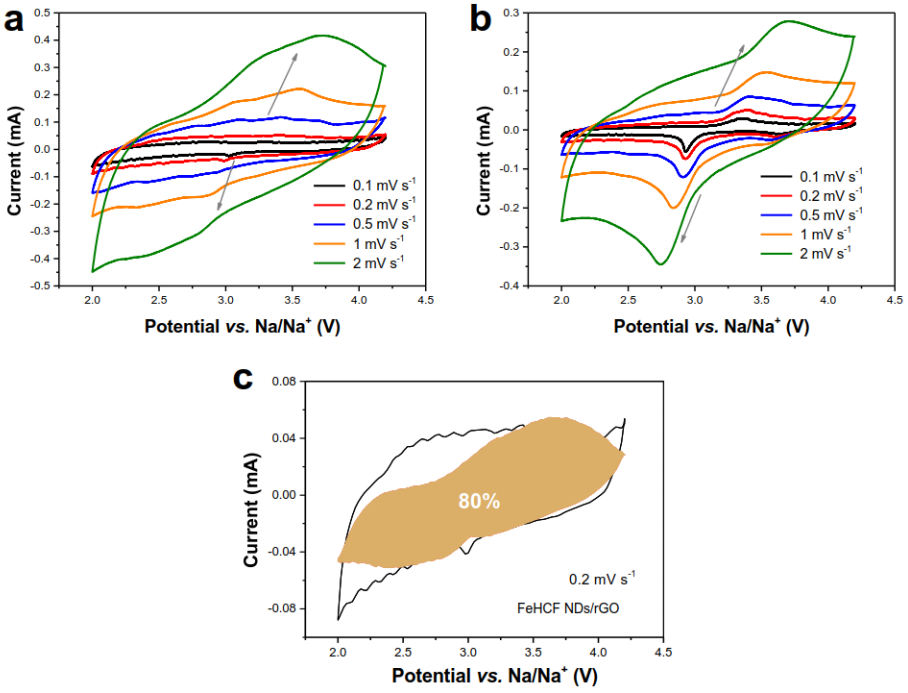

Supplementary Fig. 15 | Electrochemical reaction kinetics test. CVs of (**a**) FeHCF NDs/rGO and (**b**) FeHCF MCs/rGO at different scan rates. **c**, Separation of the capacitive and diffusion currents for FeHCF NDs/rGO at a scan rate of 0.2 mV s^{-1}.

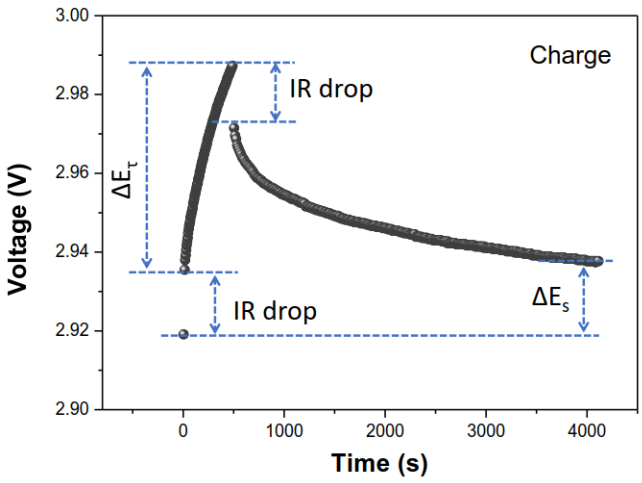

456

457 **Supplementary Fig. 16 | GITT potential response curve with time during charging.**

458

459

460

461

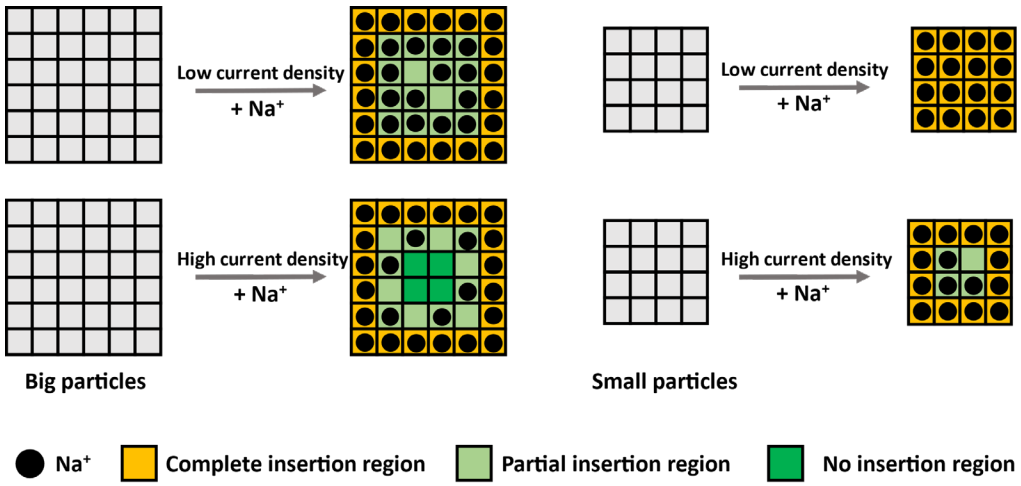

462

463 **Supplementary Fig. 17 | A sketch illustrating Na^+ diffusion in the big and small particles at both**

464 **low and high C-rates.**

465

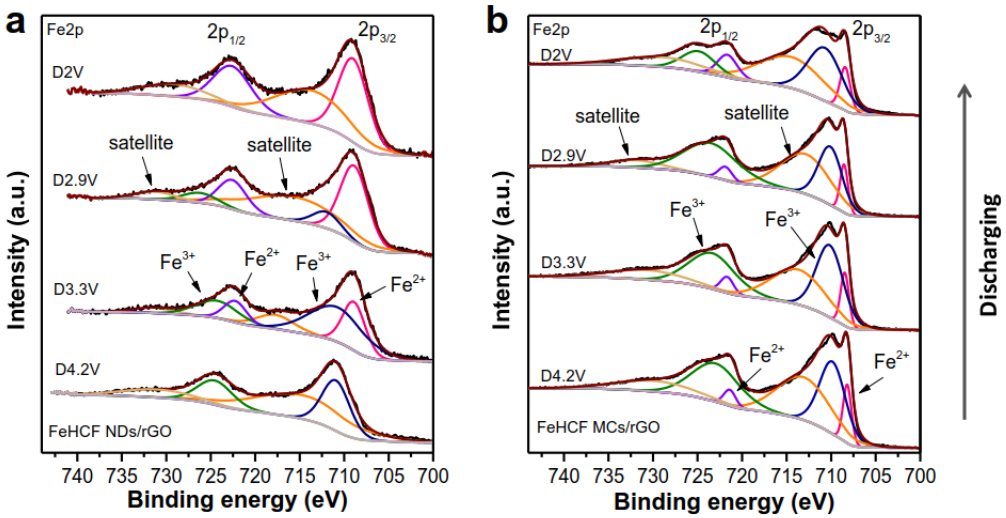

Supplementary Fig. 18 | Fe2p XPS spectra with 100 nm Ar^+ ion etching after discharge to 4.2 V, 3.3 V, 2.9 V, and 2 V. a, FeHCF NDs/rGO. **b**, FeHCF MCs/rGO. Test conditions: both electrodes were cycled at a current density of 20 C and analyzed after the 30th discharging process.

We performed XPS analyses with 100 nm Ar^+ ion etching for both electrodes after the 30th discharging process at a current density of 20 C. Because the average particle size of FeHCF MCs is 300 nm, 100 nm Ar^+ ion etching is considered to be sufficient for exposing a representative amount of the interior of the particles. Supplementary Fig. 18 shows the Fe2p spectra at different discharge states. After curve-fitting, the atomic proportions of Fe^{III} during discharging are shown in Fig. 4h and Supplementary Table 4. For FeHCF NDs/rGO, 100% of Fe^{III} found in the fully charged state (D4.2V) can be reduced to Fe^{II} after discharging, suggesting a full Na ion insertion reaction. On the other hand, for FeHCF MCs/rGO, the ratio is changed from 83.1% (D4.2V) to 71.6% (D2V), indicating that Na ion only inserted into the near-surface sites at high C-rate, so its contribution to capacity is severely decreased, and as such capacity is dominated by capacitive behavior.

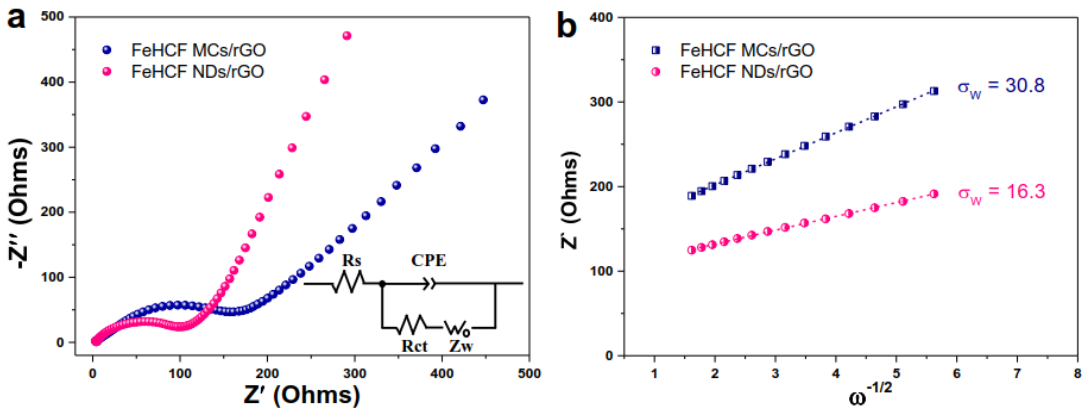

Supplementary Fig. 19 | Electrochemical impedance spectroscopy measurements. a, Nyquist plots of the two electrodes at the open circuit potential with an AC perturbation of 5 mV in the frequency range of 0.01 Hz to 100 kHz; inset is the equivalent circuit. **b**, Calculation of diffusion kinetics based on the Z′–$\omega^{-1/2}$ plot in the low-frequency region.

Electric conductivity is also crucial for high rate cathodes. Supplementary Fig. 19a shows the Nyquist plots obtained from EIS. The equivalent circuit for fitting the EIS data contains the internal resistance (Rs), the charge transfer resistance (Rct), the constant phase element (CPE), and the Warburg impedance (Zw). The diameter of the characteristic depressed semicircle in the high-frequency region is related to charge transfer resistance Rct caused by the faradaic redox process. The smaller semicircle in the high-frequency region indicates better electric conductivity of FeHCF NDs/rGO. The charge transfer resistance (R_{ct}) of FeHCF NDs/rGO and FeHCF MCs/rGO are 105 and 192 Ω, respectively. The superior conductivity of FeHCF NDs/rGO can be attributed to the strong interaction between the nanodots and graphene, and the job-sharing charge transport in the space-charge zone, which is advantageous for Na insertion/extraction at high C-rate.

In the low-frequency region, Warburg impedance could be observed from the straight line, which corresponds to the diffusion of electrolyte ions. In more detail, in a linear plot of the real (Z′) or

499 imaginary (Z'') part against the angular frequency ($\omega^{-1/2}$), the slope of this plot determines the Warburg
500 coefficient (σ_W), as shown in Supplementary Fig. 19b. Mathematically, this is expressed by:[36]

501 $$Z' = R_e + R_{ct} + \sigma_W \omega^{-1/2} \quad (12)$$

502 The diffusion coefficient (D) of electrolyte ions at the interfacial region, which is related to the Warburg
503 coefficient, is calculated by:[36]

504 $$D = 0.5(RT/An^2F^2\sigma_W C)^2 \quad (13)$$

505 The σ_W for FeHCF NDs/rGO and FeHCF MCs/rGO are 16.3 and 30.8, respectively, indicating that
506 FeHCF NDs/rGO shows much higher D value than FeHCF MCs/rGO.

507

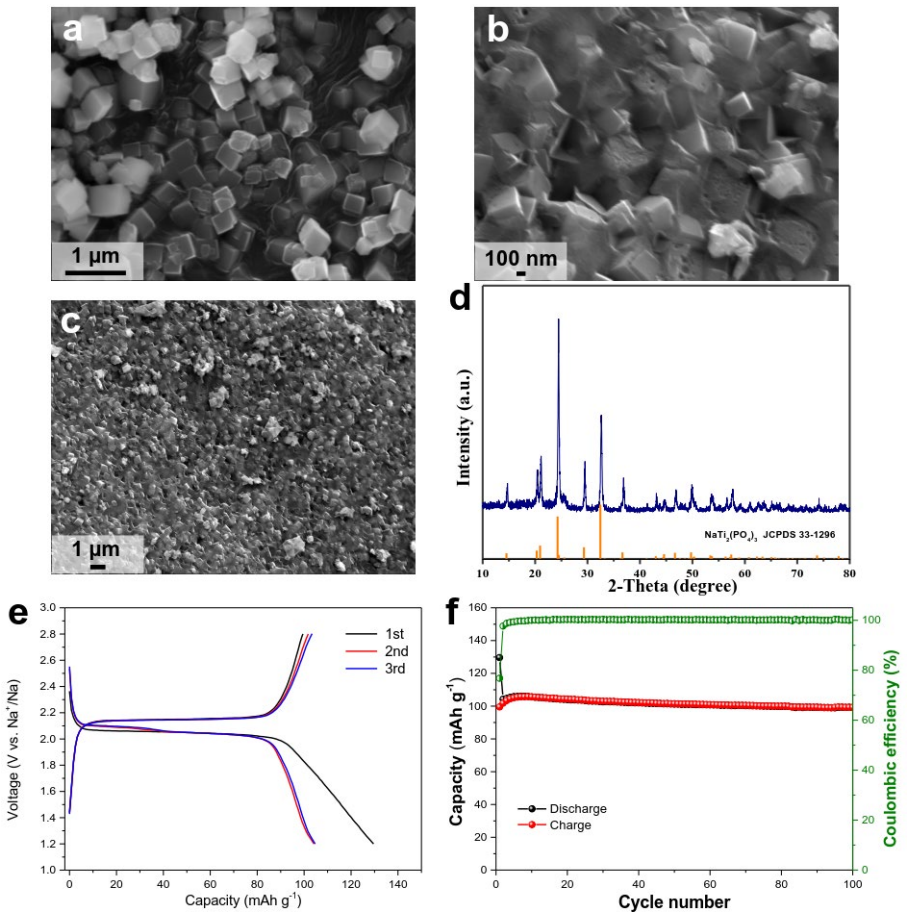

508

509 **Supplementary Fig. 20 | Characterizations and electrochemical performance of NTP@C.** SEM
510 images of (**a**) NTP and (**b**, **c**) NTP@C. **d**, XRD pattern of NTP@C. **e**, charge/discharge curves of
511 NTP@C for SIBs. **f**, cycle stability and Coulombic efficiency of NTP@C at 100 mA g^{-1}.

512

513 NTP was synthesized by a hydrothermal method. The as-prepared NTP shows a cubic morphology with a
514 size of ca. 400 nm. The carbon coating was performed through a sol-gel method followed by a
515 carbonization process. SEM images show a thin carbon layer coated on the surface of NTP cubes. The
516 XRD pattern of NTP@C matches well with the standard PDF card (33-1296) of $NaTi_2(PO_4)_3$. When used
517 as an anode for SIBs, it shows a stable discharge and charge platform at 2 V and 2.1 V. NTP@C shows
518 stable cyclability and high Coulombic efficiency, as shown in Supplementary Fig. 20f.

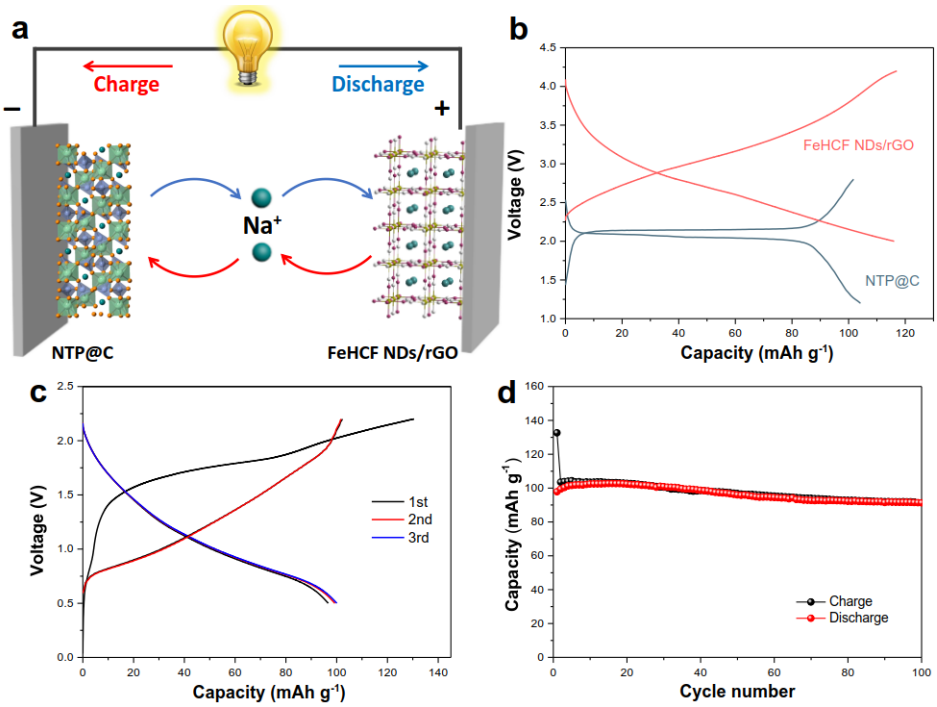

519

520 **Supplementary Fig. 21 | Electrochemical measurements of NTP@C//FeHCF NDs/rGO full cells. a**,
521 Schematic illustration of the full cells. **b**, Half-cell charge/discharge voltage curves of FeHCF NDs/rGO
522 and NTP, respectively, at a current density of 100 mA g^{-1}. **c**, Full-cell charge/discharge profiles at a
523 current density of 100 mA g^{-1}. **d**, Cycle performance at a current density of 100 mA g^{-1} (specific capacity
524 calculated by active mass of cathode material).

525

526 To demonstrate the practical applicability of this sample, a full cell was assembled by using
527 $NaTi_2(PO_4)_3$@C (NTP@C) as an anode to match with FeHCF NDs/rGO for stability tests
528 (Supplementary Fig. 21a). The voltage window was set as 0.5–2.2 V for the full cell (Supplementary Fig.
529 21b).[37] The sloping charge/discharge curve of the full cell (Supplementary Fig. 21c) within the voltage
530 range, which is probably caused by the capacitive characteristic of FeHCF NDs/rGO, is helpful to
531 monitor the state of charge (SOC) for the actually used battery.[36] The initial charge and discharge
532 capacities are 132 mAh g^{-1} and 97 mAh g^{-1}, respectively, at a current density of 100 mA g^{-1}. After 100

533 cycles (Supplementary Fig. 21d), the full cell maintains a high discharge capacity of 91 mAh g^{-1},
534 revealing the stable and reversible electrochemical reaction for both the cathode and anode. Evaluation of
535 the full cell demonstrates the potential applicability of FeHCF NDs/rGO for high-energy and high-power
536 batteries.

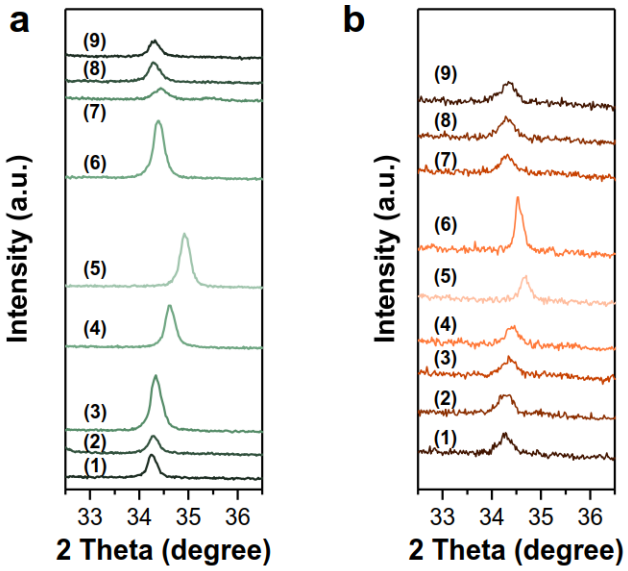

Supplementary Fig. 22 | Enlarged ex-situ XRD patterns of different electrodes during cycling. a, FeHCF MCs/rGO. **b**, FeHCF NDs/rGO.

For FeHCF MCs/rGO, the (404) peak of the R phase shifts from 34.25° to 34.92° during the charging process. For FeHCF NDs/rGO, the (404) peak of the R phase changes from 34.28° to 34.67° during the charging process. FeHCF NDs/rGO shows a smaller peak shift, revealing the smaller lattice change during cycling.

Supplementary Tables

Supplementary Table 1. Inductively coupled plasma atomic emission spectroscopy (ICP-AES) and thermogravimetric analysis (TGA) results of Fe-HCF NDs/rGO and Fe-HCF MCs/rGO.

	ICP-AES				TGA	Formula
	Na (wt%)	Fe (wt%)	Na (at%)	Fe (at%)	Interstitial water (wt%)	
Fe-HCF NDs/rGO	16.47	83.53	32.37	67.63	11.46	$Na_{0.96}FeFe(CN)_6 \cdot 2.09H_2O$
Fe-HCF MCs/rGO	15.48	84.52	30.79	69.21	10.4	$Na_{0.89}FeFe(CN)_6 \cdot 1.86H_2O$

Supplementary Table 2. Changes in lattice parameters based on XRD, vibrational modes based on Raman, and binding energy based XPS analyses for the two Prussian blue samples.

Sample	XRD			Raman (cm^{-1})				XPS Fe2p (eV)			
	2θ/(200)	a (Å)	V ($Å^3$)	$v_{Fe-CN-Fe}$	v_{Fe-C}	E_g v_{CN}	A_{1g} v_{CN}	Fe^{2+} $2p_{3/2}$	Fe^{3+} $2p_{3/2}$	Fe^{2+} $2p_{1/2}$	Fe^{3+} $2p_{1/2}$
FeHCF MCs/rGO	17.305	10.221	1067.776	276	553	2094	2155	709.07	710.58	721.91	723.69
FeHCF NDs/rGO	17.240	10.255	1078.467	269	527	2088	2149	708.72	710.33	721.52	723.41

Supplementary Table 3. Comparison of chemical resistance (R^{δ}) and chemical capacitance (C^{δ}) of traditional and "job-sharing" chemical diffusion coefficient.

	$D^{\delta} = (RT/F^2)\,(R^{\delta}C^{\delta})^{-1}$	
	$(R^{\delta})^{-1}$	$(C^{\delta})^{-1}$
Traditional bulk chemical diffusion	$\frac{\sigma_{ion}\sigma_e}{\sigma_{ion}+\sigma_e}$	$\frac{1}{c_{ion}}+\frac{1}{c_e}$
"Job-sharing" chemical diffusion	$\frac{\sigma_{ion}^{\alpha}\sigma_e^{\beta}}{\sigma_{ion}^{\alpha}+\sigma_e^{\beta}}$	$\frac{1}{c_{ion}^{\alpha}}+\frac{1}{c_e^{\beta}}+\frac{F^2s^2}{RT\varepsilon\varepsilon_0}$
Superscript: α, β: ionic conductor phase, electron conductor phase Subscript: *ion*, *e*: identifier for charge carrier σ, c: conductivity, concentration s: distance of α and β phases		

The expression of D^{δ} in bulk is given by (more details cf. reference[38])

$$D^{\delta} = \frac{RT}{F^2}\frac{\sigma_{ion}\sigma_e}{\sigma_{ion}+\sigma_e}\left(\frac{1}{c_{ion}}+\frac{1}{c_e}\right) \quad \text{(S5)}$$

The expression of D^{δ} in job-sharing interface is given by

$$D^{\delta} = \frac{RT}{F^2}\frac{\sigma_{ion}\sigma_e}{\sigma_{ion}+\sigma_e}\left(\frac{1}{c_{ion}}+\frac{1}{c_e}+\frac{F^2s^2}{RT\varepsilon\varepsilon_0}\right) \quad \text{(S6)}$$

In these equations, R^{δ} is the transport resistance that depends on the arithmetic mean of the ionic and electric resistance and C^{δ} is the chemical capacitance that depends on the ideal cases and is the harmonic mean of the ionic and electric carrier concentrations. The third term of $1/C^{\delta}$ (i.e., $\frac{F^2s^2}{RT\varepsilon\varepsilon_0}$) for the "job-sharing" chemical diffusion coefficient relates to the electrostatic energy that needs to be overcome if the concentration is changed at the heterojunction.

Supplementary Table 4. The atomic proportions of Fe^{III} at different discharged states for the two electrodes calculated from Supplementary Fig. 18.

	FeHCF NDs/rGO	FeHCF MCs/rGO
D4.2V	100%	83.1%
D3.3V	63.9%	81.6%
D2.9V	17.4%	78.6%
D2V	0%	71.6%

Supplementary References

1 Liu, J., Zheng, M., Shi, X., Zeng, H. & Xia, H. Amorphous FeOOH quantum dots assembled mesoporous film anchored on graphene nanosheets with superior electrochemical performance for supercapacitors. *Adv. Funct. Mater.* **26**, 919-930 (2016).

2 Yang, J. et al. A high-rate and ultralong-life sodium-ion battery based on $NaTi_2(PO_4)_3$ nanocubes with synergistic coating of carbon and rutile TiO_2. *Small* **11**, 3744-3749 (2015).

3 Chen, C. C. & Maier, J. Space charge storage in composites: thermodynamics. *Phys. Chem. Chem. Phys.* **19**, 6379-6396 (2017).

4 Okubo, M. et al. Nanosize effect on high-rate Li-ion intercalation in $LiCoO_2$ electrode. *J. Am. Chem. Soc.* **129**, 7444-7452 (2007).

5 Lesel, B. K., Cook, J. B., Yan, Y., Lin, T. C. & Tolbert, S. H. Using nanoscale domain size to control charge storage kinetics in pseudocapacitive nanoporous $LiMn_2O_4$ powders. *ACS Energy Lett.* **2**, 2293-2298 (2017).

6 Tang, Y. et al. Identifying the origin and contribution of surface storage in TiO_2(B) nanotube electrode by in situ dynamic valence state monitoring. *Adv. Mater.* **30**, 1802200 (2018).

7 Zhang, J. et al. Bifunctional conducting polymer coated CoP core-shell nanowires on carbon paper as a free-standing anode for sodium ion batteries. *Adv. Energy Mater.* **8**, 1800283 (2018).

8 Zhang, J. et al. Engineering solid electrolyte interphase on red phosphorus for long-term and high-capacity sodium storage. *Chem. Mater.* **32**, 448-458 (2020).

9 Hao, X. et al. Atomic-scale valence state distribution inside ultrafine CeO_2 nanocubes and its size dependence. *Small* **14**, 1802915 (2018).

10 Kuhrt, C. & Anton, R. On the origin of a lattice expansion in palladium and Pd-Au vapour deposits on various substrates. *Thin Solid Films* **198**, 301-315 (1991).

11 Wei, Z. et al. Investigation of the lattice expansion for Ni nanoparticles. *Mater. charact.* **58**, 1019-1024 (2007).

12 Srivastav, A. K., Chawake, N. & Murty, B. Grain-size-dependent non-monotonic lattice parameter variation in nanocrystalline W: the role of non-equilibrium grain boundary structure. *Scr. Mater.* **98**, 20-23 (2015).

13 Qi, W., Wang, M. & Su, Y. Size effect on the lattice parameters of nanoparticles. *J. Mater. Sci. Lett.* **21**, 877-878 (2002).

14 Abdusalyamova, M. et al. Structural features of nanocrystalline holmium oxide prepared by the thermal decomposition of organic precursors. *J. Alloys Compd.* **601**, 31-37 (2014).

15 Perebeinos, V., Chan, S.-W. & Zhang, F. 'Madelung model' prediction for dependence of lattice parameter on nanocrystal size. *Solid state commun.* **123**, 295-297 (2002).

16 Diehm, P. M., Ágoston, P. & Albe, K. Size-dependent lattice expansion in nanoparticles: reality or anomaly? *ChemPhysChem* **13**, 2443-2454 (2012).

17 Tsunekawa, S. et al. Critical size and anomalous lattice expansion in nanocrystalline $BaTiO_3$ particles. *Phys. Rev. B* **62**, 3065 (2000).

18 Bhowmik, R., Ranganathan, R. & Nagarajan, R. Lattice expansion and noncollinear to collinear ferrimagnetic order in a $MnCr_2O_4$ nanoparticle. *Phys. Rev. B* **73**, 144413 (2006).

19 Okubo, M. et al. Fast Li-ion insertion into nanosized $LiMn_2O_4$ without domain boundaries. *ACS Nano* **4**, 741-752 (2010).

20 Peck, M. A. & Langell, M. A. Comparison of nanoscaled and bulk NiO structural and environmental characteristics by XRD, XAFS, and XPS. *Chem. Mater.* **24**, 4483-4490 (2012).

21 Qi, W. & Wang, M. Size and shape dependent lattice parameters of metallic nanoparticles. *J. Nanopart. Res.* **7**, 51-57 (2005).

22 Lee, J.-H., Ali, G., Kim, D. H. & Chung, K. Y. Metal-organic framework cathodes based on a vanadium hexacyanoferrate Prussian blue analogue for high-performance aqueous rechargeable batteries. *Adv. Energy Mater.* **7**, 1601491 (2017).

23 Xie, B. et al. Achieving long-life Prussian blue analogue cathode for Na-ion batteries via triple-cation lattice substitution and coordinated water capture. *Nano Energy* **61**, 201-210 (2019).

24 Coupry, C., Lautié, A., Revault, M. & Dufilho, J. Contribution of Raman spectroscopy to art and history. *J. Raman spectrosc.* **25**, 89-94 (1994).

25 Moretti, G. & Gervais, C. Raman spectroscopy of the photosensitive pigment Prussian blue. *J. Raman Spectrosc.* **49**, 1198-1204 (2018).

26 Toulouse, J., DiAntonio, P., Vugmeister, B., Wang, X. & Knauss, L. Precursor effects and ferroelectric macroregions in $KTa_{1-x}Nb_xO_3$ and $K_{1-y}Li_yTaO_3$. *Phys. Rev. Lett.* **68**, 232 (1992).

27 Lin, T., Cong, X., Lin, M.-L., Liu, X.-L. & Tan, P.-H. The phonon confinement effect in two-dimensional nanocrystals of black phosphorus with anisotropic phonon dispersions. *Nanoscale* **10**, 8704-8711 (2018).

28 Grosvenor, A., Kobe, B., Biesinger, M. & McIntyre, N. Investigation of multiplet splitting of Fe 2p XPS spectra and bonding in iron compounds. *Surf. Interface Anal.* **36**, 1564-1574 (2004).

29 Feng, J. X. et al. Silica-polypyrrole hybrids as high-performance metal-free electrocatalysts for the hydrogen evolution reaction in neutral media. *Angew. Chem.* **56**, 8120-8124 (2017).

30 Siuzdak, K., Szkoda, M., Karczewski, J., Ryl, J. & Lisowska-Oleksiak, A. Titania nanotubes infiltrated with the conducting polymer PEDOT modified by Prussian blue–a novel type of organic–inorganic heterojunction characterised with enhanced photoactivity. *RSC Adv.* **6**, 76246-76250 (2016).

31 Balaya, P. et al. Nano-ionics in the context of lithium batteries. *J. Power Sources* **159**, 171-178 (2006).

32 You, Y., Wu, X.-L., Yin, Y.-X. & Guo, Y.-G. High-quality Prussian blue crystals as superior cathode materials for room-temperature sodium-ion batteries. *Energy Environ. Sci.* **7**, 1643-1647 (2014).

33 Song, J. et al. Removal of interstitial H_2O in hexacyanometallates for a superior cathode of a sodium-ion battery. *J. Am. Chem. Soc.* **137**, 2658-2664 (2015).

34 Kareis, C. M., Lapidus, S. H., Her, J. H., Stephens, P. W. & Miller, J. S. Non-Prussian blue structures and magnetic ordering of $Na_2Mn^{II}[Mn^{II}(CN)_6]$ and $Na_2Mn^{II}[Mn^{II}(CN)_6]\cdot 2H_2O$. *J. Am. Chem. Soc.* **134**, 2246-2254 (2012).

35 Aparicio, C., Machala, L. & Marusak, Z. Thermal decomposition of Prussian blue under inert atmosphere. *J. Therm. Anal. Calorim.* **110**, 661-669 (2012).

36 Ren, W. et al. Prussian white hierarchical nanotubes with surface-controlled charge storage for sodium-ion batteries. *Adv. Funct. Mater.* **29**, 1806405 (2019).

37 Peng, J. et al. A dual-insertion type sodium-ion full cell based on high-quality ternary-metal Prussian blue analogs. *Adv. Energy Mater.* **8**, 1702856 (2018).

38 Chen, C.-C., Navickas, E., Fleig, J. & Maier, J. Kinetics of space charge storage in composites. *Adv. Funct. Mater.* **28**, 1705999 (2018).